Flow in Packed Tubes with a Small Tube to Particle Diameter Ratio

A computer-generated slim tube randomly packed with spheres of almost uniform size is used to model single-phase flow in a packed tube with a small tube diameter to particle diameter ratio, R. To obtain a detailed description of its morphology, the slim packed tube is first tessellated into tetrahedra in the interior, and pentahedra near the walls of the tube. Then, the pore space is represented by a network of interconnected circular and triangular sinusoidal flow channels. The size and length of each channel, as well as their interconnectivity, are exactly known. In addition, porosity and solid surface area per unit volume of the porous medium are determined as a function of distance away from a wall. These data suggest that the presence of the walls has two counteracting effects on fluid flow. A higher porosity promotes flow along the walls but a higher surface area per unit volume hinders it. To confirm this prediction, experimental permeability data are obtained for tubes with R between 2.5 and 40. For $R > 25$, the permeability is the same as that of a large diameter tube, k_∞. Between 8 and 25, the permeability can be larger or less than k_∞. The way the tube is packed determines whether the higher porosity or surface area dominates in the wall region, and thus higher or lower permeability. Below $R = 8$, the confining walls cause a marked increase in overall bed porosity and the permeability is always larger than k_∞. Theoretical predictions of the permeability of such very slim tubes are in good agreement with experimental data.

C. F. Chu, K. M. Ng
Department of Chemical Engineering
University of Massachusetts
Amherst, MA 01003

Introduction

Darcy's law is widely used for laminar, single-phase flow in porous media. It suggests a linear relationship between the volumetric flow rate of the fluid Q and the pressure gradient ∇p, that is,

$$\frac{Q}{A} = \frac{k}{\mu} |\nabla p| \tag{1}$$

Here, A is the cross-sectional area for fluid flow and μ is the viscosity. The permeability k is only a function of the geometry and topology of the porous structure. Various experimental correlations based on parameters such as the size of the packing particles and porosity are available for estimating the value of k (Bird et al., 1960; Dullien, 1975, 1979). In addition, there exist a large number of models with various degrees of sophistication for predicting the permeability (Dullien, 1979).

Although one can insist on using Darcy's law to describe flow in a packed slim tube where only a limited number of packing particles can be accommodated within the relatively small cross section, none of the existing correlations, which are based on large diameter tubes, provides the correct permeability. It is well known that the porosity in the region next to the containing walls of a packed tube is higher than that in the remainder of the bed. To be more exact, the porosity has a limiting value of unity at the wall and then its magnitude oscillates with decreasing amplitude away from the wall (Benenati and Brosilow, 1962). (The limiting value is associated with an annular shell of infinitesimal thickness next to the wall.) Apparently, the failure of the correlations is a manifestation of this wall effect, which becomes increasingly dominant as the ratio of tube diameter to particle diameter decreases ($R = D/d_s$). The flow field, in turn,

Correspondence concerning this paper should be addressed to K. M. Ng.

is significantly different from that in a tube with sufficiently large R.

Flow in a packed slim tube is of considerable interest. For example, o-xylene oxidation to phthalic anhydride and production of ethylene oxide from ethylene, both highly exothermic catalytic reactions, are carried out in packed slim tubes surrounded by a heat exchanger medium. Only a few particles can fit across the tube so that rapid heat removal through the walls is possible (Dixon et al., 1984; Melanson and Dixon, 1985). Furthermore, flow in the wall region can be of significance even in tubes of large R. It can affect the wall heat transfer coefficient (Dixon and Cresswell, 1979; Dixon, 1985), and flow distribution and conversion in large-scale packed-bed reactors (Choudhary et al., 1976; Lerou and Froment, 1977).

A number of theories have been proposed in the literature to incorporate the wall effect in flow through porous media. Cohen and Metzner (1981) suggested a triregional model—a wall region next to the tube walls, a bulk region along the center of the tube, and a transition region in between. Each region is considered to be made up of parallel capillary tubes, the hydraulic radius of which varies according to an experimentally measured porosity profile away from the wall. An alternative two-zone model was discussed by Nield (1983). A thin layer of a uniform thickness on the order of one particle diameter adjacent to the wall is assumed to be occupied by fluid only. This is followed by the packed bed, which is assumed to be of uniform porosity and thus can be described by Darcy's law. The boundary condition introduced by Beavers and Joseph (1967) is used to complete the analysis of this two-region model. Vortmeyer and Schuster (1983) opted for the Brinkman equation, using essentially the Ergun equation modified with a viscous term to account for any boundary effect.

The empirical nature of the Beavers and Joseph boundary condition and the Brinkman equation is well known, although considerable progress has been made to elucidate the physics as well as the limitations (Taylor, 1971; Richardson, 1971; Koplik et al., 1983; Wilkinson, 1985; Larson and Higdon, 1986). With empiricism aside, a common disadvantage of the current wall effect models is that the predictions are not sufficiently detailed for some applications. For example, radial fluid flow is a significant contributing factor to heat transfer in a packed slim tube (Dixon et al., 1984) but all three models above are limited to axial, one-dimensional flow.

These wall effect models, however, provide significant insights into the wall effect phenomenon. Arguing that the tube walls have a restrictive effect on flow, both Cohen and Metzner (1981), and Nield (1983) predicted that the apparent permeability decreases for decreasing values of the bed to particle diameter ratio. This is in agreement with the data reported by Coulson (1949), Rose (1945), and Mehta and Hawley (1969), which were primarily based on tubes with R on the order of 10 or above. Indeed, no data seem to exist for R less than 6.4. Interestingly, as pointed out in a discussion between Cohen and Nield (1985), Nield's model can indeed predict that the apparent permeability increases with decreasing R, as indicated by the data of Furnas (1929), if the wall zone is sufficiently thick in the two-zone model. We will return to this point at a later stage.

The objective of this study is to offer a new model for single-phase flow in a slim tube randomly packed with spheres of almost uniform size. Emphasized are slim tubes with a small tube to particle diameter ratio, particularly for tubes with R less than 10. As mentioned, there is a paucity of experimental data for permeability in such very slim tubes. A simple and easy-to-use experimental setup is developed to provide the necessary data. As will be seen below, the data provide support to a phenomenon previously unconfirmed in the literature.

It should be mentioned that numerous analyses for flow through sphere packs exist. There are solutions for flow in regular sphere packs (Snyder and Stewart, 1966; Sørensen and Stewart, 1974; Zick and Homsy, 1982; Lahbabi and Chang, 1985), for models with flow over a single sphere (Neale and Nader, 1974), and for models with flow in a constricted channel between spherical particles (Payatakes et al., 1973; Payatakes and Neira, 1977). None is available for an actual random sphere pack, not to mention one with the wall effect present.

In modeling transport phenomena in porous media, it is essential to quantify the geometrical characteristics of the medium such as connectivity, shape and size of the pore chambers, and other characteristics relevant to the analysis of the physical problem under consideration. For this reason, there exist a large number of porous medium models; most of the earlier models have been reviewed by van Brakel (1975). However, little is known about the pore chambers next to the confining walls. This is probably the reason why both Cohen and Metzner (1981) and Vortmeyer and Schuster (1983) used the oscillating porosity profile in their models, as it is the only information available about the wall effect. It is not surprising, therefore, that this study begins with a more detailed porous medium model.

Porous Medium Model

It is not an easy task to obtain detailed information about the pore chambers in the wall region of an actual packed tube; computer simulation provides an attractive alternative. Such a computer-generated packed tube is briefly described below.

We begin with an empty tube with a square cross section. Spheres of a given particle size distribution are dropped one by one from a random position at the top into the tube. In this study, we use a narrow distribution to simulate spheres of almost the same size. All collisions are assumed to be inelastic. If the sphere hits the bottom of the tube, it stays at the position where it lands. If the sphere hits another sphere already inside the tube, it rolls under gravity. It stops only after reaching a stable position, such as resting on top of three other spheres or on top of two spheres while leaning against a wall. Statistical results such as coordination number, number of circles irrespective of size per unit horizontal sectional plane, and others indicate that the model is a realistic one (Chan and Ng, 1986).

Tetrahedral and pentahedral units

To obtain the geometrical characteristics of the pore space, tetrahedral tessellation is first applied to the sphere pack itself. Then, pentahedral tessellation is applied to the space between the walls and the spheres. The vertices of each tetrahedron are the centers of four neighboring but not necessarily touching spheres. Starting with a seed tetrahedron, tetrahedra are added one at a time to the existing cluster of tetrahedra. The algorithm ensures that only close-to-regular tetrahedra are considered. The end product is a cluster of nonoverlapping and space-filling tetrahedra that encompasses all the spheres in the tube. A pore chamber is the void space within a tetrahedron and a pore throat is the areal void space on a triangular surface common to two

contiguous tetrahedra, as shown in Figure 1. Data for the pore size distribution, constriction size distribution, and other factors are reported by Chan and Ng (1988).

In this study, we extend the existing code for the previous work to consider the wall effect. To be concise, let us examine a bin packed with 256 spheres having a uniform size distribution ranging from 0.95 to 1 (arbitrary unit) in radius. The square cross section has a width of 10 radii of the largest sphere. Figure 2 shows what the cluster of tetrahedra looks like from the top, the bottom, or the four walls—front, back, left, and right. The origin $x = y = 0$ is located at the junction of the front and left walls. Consider one of the triangles on a wall, ΔABC. It represents the projection on the wall of a triangle on the external surface of the tetrahedron cluster, ΔEFG, Figure 3. Note that the vertices of ΔEFG are the centers of three spheres, which are not necessarily touching the wall, that is, the plane on which ΔABC lies. The pentahedral unit, like the tetrahedral unit, is a natural choice for tessellation as it has several throats leading to a relatively large pore. The wall pore chamber is the void space within the pentahedral unit. There are four pore throats. The throat on EFG connects the wall pore chamber to an interior pore chamber within the cluster while the other three are linked to other wall pore chambers.

Figure 4 shows some statistics of these pentahedral units for this 10 × 10 × 20 sphere pack. Figure 4a is a histogram for the average length of the three parallel edges of the pentahedron, $\langle d_w \rangle$. Recall that the sphere radius ranges from 0.95 to 1. Since $\langle d_w \rangle$ is generally larger than unity, not all three spheres are in touch with the vertical wall. Indeed, the ratio of the largest d_w to the smallest in a given pentahedral unit can be larger than 3, Figure 4b. The porosity of a pentahedral unit, ϵ_w, is defined as the void volume in a pentahedral unit divided by the total volume of the same. A similar definition can be made for the porosity of a tetrahedral unit, ϵ_t. The porosity of these pentahedral units ranges from 0.35 to 0.85, with a mean value of 0.578, Figure 4c. It is interesting to compare Figure 4c to Figure 5, which shows the porosity distribution of the tetrahedra. The mean value of 0.387 for the interior porosity of the bed is significantly lower than that of the wall region.

Porosity profile and surface area per unit volume

Two other pieces of information are also of interest. Figure 6 shows the porosity profile as a function of distance from the wall on the vertical plane $y = 10$ for a system with a cross section of 20 × 20. The profile ends at the center of the tube since the other half is more or less symmetric to what is shown. The curve represents line porosity values and the method of calculation is discussed by Chan and Ng (1986). The porosity has a limiting value of unity at the wall where only sphere-wall contact points are present. As expected, the first minimum in porosity occurs at about one particle radius away from the wall. Then the porosity profile oscillates and the minima occur at less predictable positions as the spheres become more uniformly mixed.

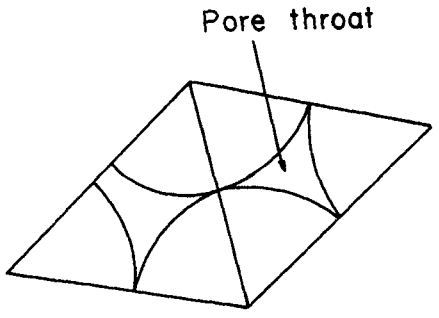

Figure 1. Tetrahedral unit made up of four spheres.
Indicated pore throat is on a face of the tetrahedron

Also shown in Figure 6 is the surface area per unit volume, A_v. There are 10 data points (not shown) on the solid curve, one for each division on the x axis. Each data point is the mean value over a slab, one particle radius in width along x, 20 radii in length along y, and a height that is the mean height of all the spheres at the very top of the packing. The solid curve does not include the area of the wall at $x = 0$ while the broken line does. Clearly, the wall area cannot be neglected as it serves as a momentum sink in flow in porous media.

Thus, the geometrical characteristics of the packed tube suggest that the wall effect has two opposite effects on flow in slim tubes packed with spheres. A higher porosity promotes flow along the wall region but a higher surface area per unit volume hinders it. If porosity is the dominant effect on flow, the permeability in a slim tube would be higher than that in a large tube. The opposite is true if surface area effect dominates. These competing effects can be quantified as follows.

Interior and wall flow channels

With tetrahedral tessellation and the subsequent formation of pentahedra in the wall region, almost the entire space within the square tubes is filled with these units. The only exception is the open space at the four corners of the tube. To eliminate this corner space, we assume that wall pore chambers located along the corner region on one wall are connected to the corresponding wall pore chambers on the connecting wall. To be specific, consider the front wall in Figure 2c. There are nine wall pore throats close to $x = 0$, indicated by the lines 12, 23, and so on, which are open to the corner. There are nine corresponding wall pore throats close to $y = 0$ on the left wall, Figure 2e. These corresponding wall chambers are assumed to be linked as if the space at the corner did not exist. Thus, the space at the four corners does not participate in the flow simulation. The next step is to identify the flow channels among these interconnected tetrahedra and pentahedra.

As mentioned, each tetrahedral unit has one pore chamber and four pore throats. The equivalent radius of a pore chamber, r_p, can be calculated from the void space within that pore as

$$r_p = \left(\frac{3\epsilon_t V_t}{4\pi}\right)^{1/3} \tag{2}$$

where V_t is the volume of the tetrahedral unit and ϵ_t is its porosity. The equivalent radius of one of the pore throats, or constrictions, r_c, can be defined as

$$r_c = \left(\frac{A_c}{\pi}\right)^{1/2} \tag{3}$$

and the hydraulic radius, r_{ch}, as

$$r_{ch} = \frac{2A_c}{S_{sl}} \tag{4}$$

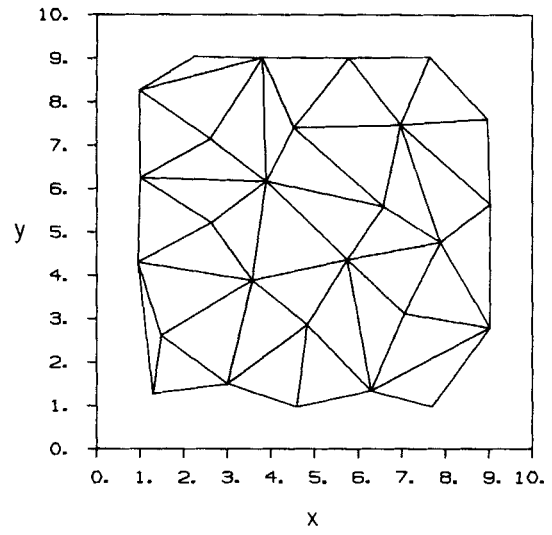

2a. Top.

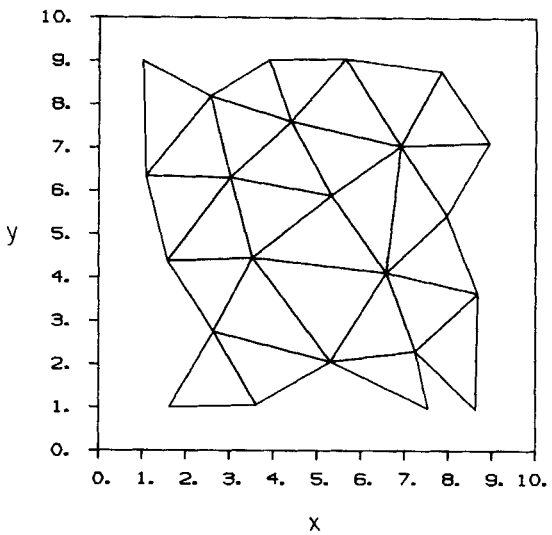

2b. Bottom.

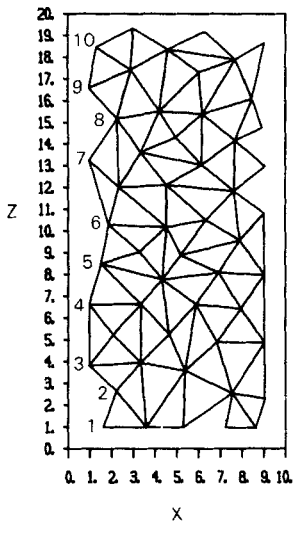

2c. Front wall.

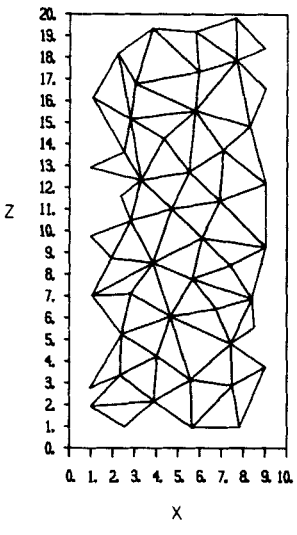

2d. Back wall.

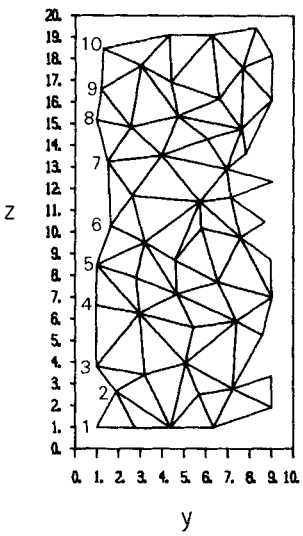

2e. Left wall.

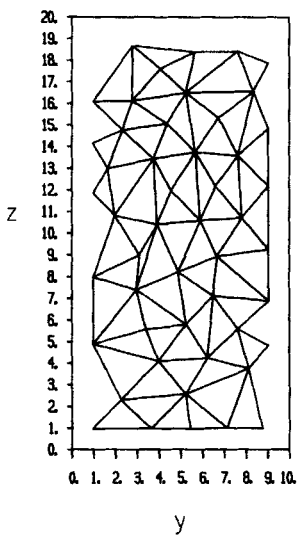

2f. Right wall.

Figure 2. Projections of cluster of tetrahedra on the top, bottom, and walls of a square column.

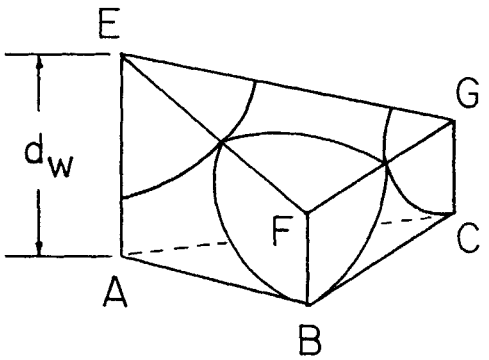

Figure 3. Pentahedral unit made up of three spheres and a vertical wall.

where A_c is the areal void space on the triangular surface of the tetrahedron and S_{sl} is the length of the solid-fluid boundary.

Following Payatakes et al. (1980), we assume that each pair of adjacent tetrahedral pores is connected by a circular tube with a sinusoidal wall profile,

$$r(z) = \frac{1}{2}(r_p + r_c)\left(1 - b\cos\frac{\pi z}{l}\right) \tag{5}$$

where $b = (r_p - r_c)/(r_p + r_c)$ and l is half of the wavelength of the sinusoidal tube. Since two adjacent pores are generally of different sizes, the sinusoidal tube is not necessarily symmetric, Figure 7. Each pore chamber is made up of four halves of these sinusoidal tubes. The length l is chosen to be the distance between the centroid of the tetrahedron and the centroid of the triangular face under consideration. We insist that the total vol-

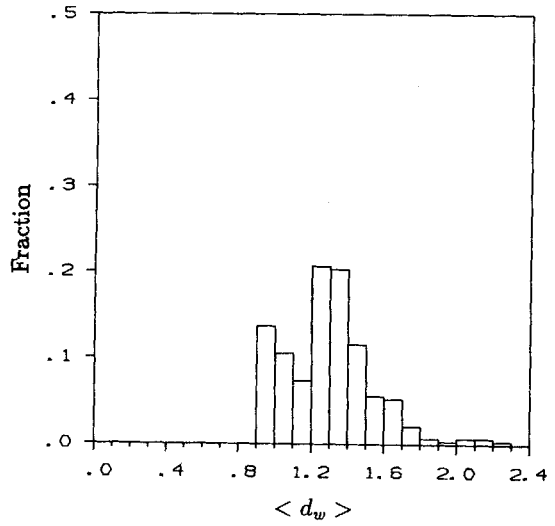

4a. Average length of parallel edges.

4b. Edge length ratio.

4c. Porosity.

Figure 4. Histograms of pentahedral unit factors.

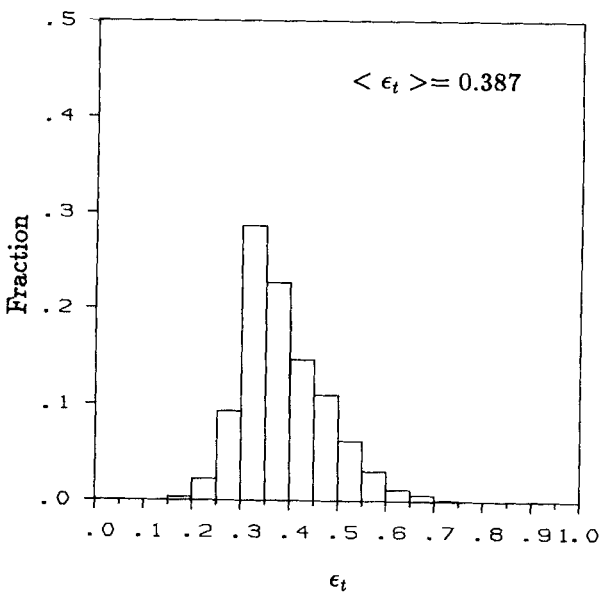

Figure 5. Distribution of porosity of tetrahedral units.

ume of these half-sinusoidal tubes be equal to the pore space,

$$\sum_{i=1}^{4} V_{ct,i} = \epsilon_t V_t \tag{6}$$

In general, the lefthand side of Eq. 6 is greater than the right-hand side if the full value of l for each half-sinusoidal tube is used. To satisfy Eq. 6, the half-sinusoidal tubes to a given pore chamber are shortened by the same fraction f of the original length at the pore chamber end. The volume of a shortened half-circular sinusoidal tube is given by

$$V_{ct} = \frac{(r_p + r_c)^2 l}{4}\left[f\pi\left(1 + \frac{b^2}{2}\right) - 2b \sin f\pi + \frac{b^2}{4}\sin 2f\pi\right] \tag{7}$$

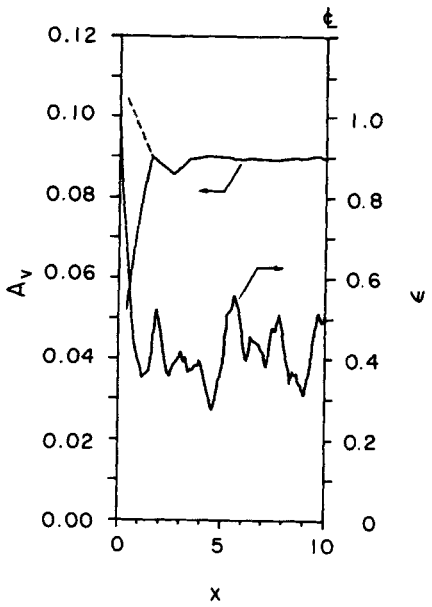

Figure 6. Bed porosity profile and surface area per unit volume as a function of lateral position.

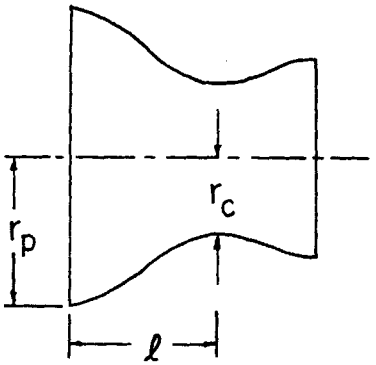

Figure 7. Circular sinusoidal tube.

The fraction f is determined from Eq. 6 for each interior pore chamber.

Let us turn our attention to the pentahedral unit, Figure 3. We propose that the pore chamber of the pentahedral unit is made up of a half-circular sinusoidal tube and three half-sinusoidal tubes whose cross sections are equilateral triangles, Figure 8. The circular tube leads to a tetrahedral unit while the triangular tubes lead to other pentahedral wall units. We assume that the three triangular sinusoidal tubes within the same wall pore chamber have a common height given by

$$h_{pw} = \langle d_w \rangle - \frac{d_g}{4} \tag{8}$$

The equivalent height of each of the constrictions, h_{cw}, can be defined as

$$h_{cw} = (\sqrt{3}A_{cw})^{1/2} \tag{9}$$

and the hydraulic height, h_{cwh}, as

$$h_{cwh} = \frac{6A_{cw}}{S_{sl}} \tag{10}$$

where A_{cw} is the cross-sectional area of the constriction and S_{sl} is the length of the solid-fluid boundary. The height of the triangular sinusoidal tube changes along the axial direction, z, and is given by

$$h(z) = \frac{1}{2}(h_{pw} + h_{cw})\left(1 - c\cos\frac{\pi z}{l}\right) \tag{11}$$

where $c = (h_{pw} - h_{cw})/(h_{pw} + h_{cw})$ and l is half of the wavelength of the triangular sinusoidal tube. The length l is chosen to be the

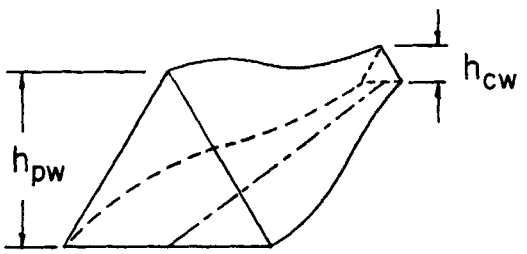

Figure 8. Triangular sinusoidal tube.

distance between the centroid of the base triangle (such as ΔABC in Figure 3) and the centroid of the edge under consideration (such as BC in Figure 3). Again, we insist that the total volume of the triangular tubes and the circular tube be equal to the pore space within the pentahedral unit,

$$\sum_{i=1}^{3} V_{tt,i} + V_{ct} = \epsilon_w V_w \tag{12}$$

In general, the lefthand side of Eq. 12 is greater than the righthand side if the full value of l for each triangular tube is used. To satisfy Eq. 12, the triangular tubes are shortened by the same fraction g of the original length at the pore chamber end. The volume of a shortened triangular sinusoidal tube is given by

$$V_{tt} = \frac{(h_{pw} - h_{cw})^2 l}{4\sqrt{3}\pi}\left[g\pi\left(1 + \frac{c^2}{2}\right) - 2c\sin g\pi + \frac{c^2}{4}\sin 2g\pi\right] \tag{13}$$

The fraction g is determined from Eq. 12 for each wall pore chamber.

Single-Phase Flow

Flow through the sinusoidal tubes

The volumetric flow rate through a cylindrical flow channel can be calculated using the Poiseuille equation:

$$q = \frac{\pi r^4}{8\mu}\frac{\Delta p}{\Delta z} \tag{14}$$

The lubrication approximation can be applied to extend Eq. 14 to calculate low Reynolds number flow in a circular sinusoidal tube provided that the curvature of the channel profile changes gradually. This is not exactly valid in a packed bed although it is a reasonable approximation (Sheffield and Metzner, 1976). Substituting $r(z)$ from Eq. 5 into the differential form of Eq. 14 and integrating along the axial direction from 0 to ℓ, we get

$$\Delta p = \frac{128\mu q}{\pi(r_c + r_p)^4}\int_0^{\ell}\frac{dz}{\left(1 - b\cos\frac{\pi z}{l}\right)^4} \tag{15}$$

Equation 15 can then be written in the following form,

$$q = g_{ct}\Delta p \tag{16}$$

where g_{ct} is the flow conductance of the shortened sinusoidal tube and its inverse is given by

$$\begin{aligned}\frac{1}{g_{ct}} = \frac{128\mu l}{\pi^2(r_{ch} + r_{ph})^4}\Bigg\{&\frac{b'}{3(1-b'^2)}\frac{\sin f\pi}{(1 - b'\cos f\pi)^3} \\ &+ \frac{5b'}{6(1-b'^2)^2}\frac{\sin f\pi}{(1 - b'\cos f\pi)^2} \\ &+ \frac{b'(11 + 4b'^2)}{6(1-b'^2)^3}\frac{\sin f\pi}{(1 - b'\cos f\pi)} \\ &+ \frac{2 + 3b'^2}{(1-b'^2)^{7/2}}\left[\tan^{-1}\frac{\sqrt{1-b'^2}\tan\frac{f\pi}{2}}{(1-b')}\right]\Bigg\}\end{aligned} \tag{17}$$

Here, $b' = (r_{ph} - r_{ch})/(r_{ph} + r_{ch})$. Note that hydraulic radii have replaced the equivalent radii of the pore and constrictions in order to fully reflect the flow resistance. The constriction hydraulic radius is defined in Eq. 4. The pore hydraulic radius for a given shortened circular sinusoidal tube is calculated as

$$r_{ph} = \left(\frac{r_{ch}}{r_c}\right) r_p \tag{18}$$

The volumetric flow rate-pressure drop relationship for a conduit with an equilateral triangle cross section and height h is

$$q = \frac{\sqrt{3}}{180} \frac{h^4}{\mu} \frac{\Delta p}{\Delta z} \tag{19}$$

Following the same procedure for the circular sinusoidal tube, we obtain for a shortened triangular tube,

$$q = g_{tt} \Delta p \tag{20}$$

and

$$\frac{1}{g_{tt}} = \frac{180\mu l}{\sqrt{3}\left(\frac{h_{cwh} + h_{pwh}}{2}\right)^4} \left\{ \frac{c'}{3(1 - c'^2)} \frac{\sin g\pi}{(1 - c' \cos g\pi)^3} + \frac{5c'}{6(1 - c'^2)^2} \frac{\sin g\pi}{(1 - c' \cos g\pi)^2} + \frac{c'(11 + 4c'^2)}{6(1 - c'^2)^3} \frac{\sin g\pi}{(1 - c' \cos g\pi)} + \frac{2 + 3c'^2}{(1 - c'^2)^{7/2}} \left[\tan^{-1} \frac{\sqrt{1 - c'^2} \tan \frac{g\pi}{2}}{(1 - c')} \right] \right\} \tag{21}$$

Here, $c' = (h_{pwh} - h_{cwh})/(h_{pwh} + h_{cwh})$ and h_{pwh} is calculated in a manner similar to Eq. 18.

Flow through the bed

In simulating flow through the computer-generated sphere pack, the fluid is introduced at the top of the column. In other words, the external triangular faces facing the top, Fig. 2a, and the wall pore throats at the top of the four walls, Figures 2c to 2f, receive input fluid. The fluid flows from one pore chamber to another until it reaches the bottom of the column. If the total flow rate and the applied pressure gradient are known, the permeability can be calculated from Eq. 1.

Method of Solution

Once all the flow channels and associated conductances are identified, the pressure distribution in the computer-generated sphere pack can be determined as follows. If the fluid is incompressible, conservation of mass at each node, that is, either an interior or wall pore chamber, requires that

$$\sum_j (p_j - p_i) g_{ij} = 0 \tag{22}$$

Here, the summation is carried out over all the channels leading to node i and g_{ij} is calculated with either Eq. 17 or Eq. 21.

Based on the same idea, the node analysis in electrical circuit theory (Desoer and Kuh, 1969, Ng and Payatakes, 1985) provides a more compact set of equations

$$\boldsymbol{G}\boldsymbol{p} = \boldsymbol{J} \tag{23}$$

Here, $\boldsymbol{p}$ is the nodal pressure vector. The equivalent flow rate vector $\boldsymbol{J}$ represents the applied pressure difference. The conductance matrix $\boldsymbol{G}$ is sparse but not symmetric, and it is a function of the detailed pore structure. A diagonal element, G_{ii}, is the summation of the conductances of the flow channels attached to node i, while an off-diagonal element G_{ij} is the conductance of the flow channel from node j to node i. Equation 23 is a linear system and can be solved by Gauss elimination. Once the pressure distribution is obtained, the flow rate across a constriction can be calculated easily by multiplying the pressure drop and conductance.

Simulation Algorithm

To determine the permeability of a slim tube, we follow these steps:

1. Generate a random packed bed with the desired column to particle diameter ratio.
2. Identify the constrictions and pore chambers through tetrahedral tessellation.
3. Identify the pentahedral wall units by projecting the external triangular faces to the four walls.
4. Number the constrictions and pore chambers for the interior and wall units.
5. Determine the connectivity among all the pore chambers.
6. Calculate the size of all constrictions and pore chambers.
7. Calculate the conductance of all the circular and triangular sinusoidal tubes.
8. Generate the conductance matrix, $\boldsymbol{G}$.
9. Apply a pressure drop across the column.
10. Solve Eq. 23 for the pressure distribution through Gauss elimination.
11. Calculate the fluid flow rate for all flow channels.
12. Calculate the total flow rate through the bed, Q, and then the permeability with Eq. 1.
13. Change the bed size and repeat steps 1 to 12.

Experimental Method

Apparatus

A simple and easy to operate experimental setup was used to determine the apparent permeability of a slim tube packed bed. It comprised a cylindrical tube packed with spheres to a height of L, two burettes with valves removed, and a separate valve, Figure 9. The burettes were connected to both ends of the column by rubber tubings. Water was chosen as the fluid for these flow experiments. The necessary pressure head was obtained by adjusting the water level in the burettes. A fritted glass disk of pore size 25–50 μm was used as a support for the spheres at the bottom of the column.

The tube and burette diameters were determined before use. The cross-sectional area of each burette was determined by adding a known amount of water into the burette and measuring the rise in water level. The inner diameter of the tube was in turn

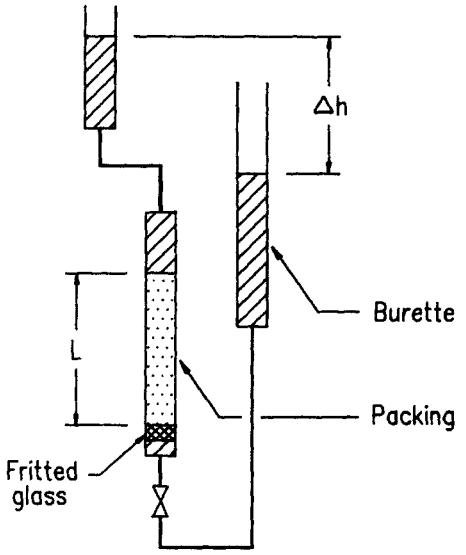

Figure 9. Experimental apparatus.

determined by allowing water to flow from a burette to the tube and measuring the change in water level after equilibrium was reached. In addition, the inner diameter value was confirmed by adding (withdrawing) a known amount of water into (from) the tube.

Six different tubes and nine particle sizes were used in these experiments to provide different values of the tube to particle diameter ratio. The length of the tubes was 50 cm, and the inner diameters were 0.273, 0.491, 0.802, 0.957, 1.546, and 1.890 cm. The tubes were packed with spherical glass beads (Potters Industrial, Inc.) ranging from 0.024 to 0.160 cm in diameter.

Procedure

The experimental procedure was rather straightforward. The tube and the burette connected to the lower end of the tube were first filled with water. Glass beads, after being weighed with an electronic balance, were then added slowly into the cylindrical tube. Care was exercised to ensure that air bubbles were not trapped inside. The tube was tapped periodically to enhance settling to a final packing length of L. Since the glass beads have a density of 2.5 g/cm^3, the bed porosity could easily be calculated. Another burette was then connected to the upper end of the tube and filled with water. By adjusting the positions of the burettes, an initial hydrostatic head of $\Delta h(t_o)$ was obtained. The valve was then opened to allow water flow through the packed tube to a final head of $\Delta h(t)$ in a period of t. To ensure reproducibility, this step was repeated at least three times. The entire experiment was then repeated for two more different packing lengths. This procedure was followed for all combinations of the six tubes and nine particle sizes.

Data analysis

If we apply a hydrostatic head, Δh, to the experimental system, the resistance to the flow is due to the packed tube as well as the valve, rubber tubings, and the fritted glass disk. Let α represent the combined resistances due to the miscellaneous items except the packed tube. If the Reynolds number is sufficiently low, one can invoke the pseudosteady assumption and rewrite Darcy's law, Eq. 1, as

$$Q(t) = \frac{\rho g \Delta h(t)}{\left(\frac{L}{Ak} + \alpha\right)\mu} \tag{24}$$

The volumetric flow rate, $Q(t)$, and pressure head, $\Delta h(t)$, are functions of time. Let V be the volume of liquid passed through the packed tube from t_o to t. By mass balance,

$$V(t) = \int_0^t Q(t')\,dt' \tag{25}$$

The pressure head $\Delta h(t)$ is given by,

$$\Delta h(t) = \Delta h(t_o) - \frac{2V(t)}{A_b} \tag{26}$$

where A_b is the cross-sectional area of the burettes. Substituting Eqs. 25 and 26 into Eq. 24 we get

$$Q(t) = \frac{\rho g}{\left(\frac{L}{Ak} + \alpha\right)\mu}\left[\Delta h(t_o) - \frac{2}{A_b}\int_0^t Q(t')\,dt'\right] \tag{27}$$

Differentiating Eq. 27 and applying the Leibnitz rule, we get

$$\frac{dQ(t)}{dt} = -\frac{2}{A_b}\frac{\rho g}{\left(\frac{L}{Ak} + \alpha\right)\mu}Q(t) \tag{28}$$

Integration of Eq. 28 yields,

$$\frac{Q(t)}{Q(t_o)} = \exp\left[-\frac{2}{A_b}\frac{\rho g t}{\left(\frac{L}{Ak} + \alpha\right)\mu}\right] \tag{29}$$

It can be seen in Eq. 24 that

$$\frac{Q(t)}{Q(t_o)} = \frac{\Delta h(t)}{\Delta h(t_o)} \tag{30}$$

Therefore, combination of Eqs. 29 and 30 yields

$$\frac{L}{Ak} + \alpha = \frac{2}{A_b \mu}\frac{\rho g t}{\ln\frac{\Delta h(t_o)}{\Delta h(t)}} \tag{31}$$

Because data are obtained for three different packing lengths, the resistance α can be eliminated from data of any two different packing lengths, L_1 and L_2. The permeability is given by

$$k = \frac{A_b \mu (L_1 - L_2)}{2A\rho g\left\{\left[\frac{t}{\ln\frac{\Delta h(t_o)}{\Delta h(t)}}\right]_1 - \left[\frac{t}{\ln\frac{\Delta h(t_o)}{\Delta h(t)}}\right]_2\right\}} \tag{32}$$

Results and Discusssion

Figure 10 shows the dependence of the measured and predicted apparent permeability on the tube to particle diameter ratio. The apparent permeability is normalized with the permeability for an infinite porous medium as predicted by the Blake-Kozeny equation (Bird et al., 1960),

$$k_\infty = \frac{d_g^2}{150\mu}\frac{\epsilon^3}{(1-\epsilon)^2} \tag{33}$$

It should be emphasized that a bed porosity value corresponding to an infinite column should be used in Eq. 33.

Let us first consider in detail the experimental data in the plot. There are a total of 41 data points, indicated by the unfilled symbols. Each symbol corresponds to a given particle size. Of course, the size of the tube for a specific data point can be inferred from the corresponding value of R. If there are two identical symbols for a given R, it means that we repeated that tube-particle size combination twice. It can be seen in the six repeated experiments that an experiment is not exactly reproducible. The difference in the k/k_∞ value is due to the fact that repacking the tube can cause slight variations in bed porosity. We will come back to this point at a later stage. Despite the lack of total reproducibility, the data hover around unity for large R and exhibit a definite upward trend for R less than around 7 or 8. The k/k_∞ value is around 2.5 when R is close to 2.7. Although we did not get more data beyond this point, k/k_∞ would be equal to zero at $R = 1$, as a single spherical particle would completely plug up the tube.

The significant increase in k/k_∞ is not at all surprising when one examines the experimental data of bed porosity as a function of R, Figure 11. Beginning at around 0.38 for R larger than 30, the porosity increases gradually with decreasing R and then exhibits a more pronounced upward trend for R less than, again, about 7 or 8. The increase in apparent permeability coincides with the increase in porosity, and this clearly indicates that one leads to the other.

Based on the discussion in the Introduction, the reader might have already concluded that this phenomenon of an increase in apparent permeability at very low R has not been clearly confirmed in the literature. In fact, the apparent permeability was

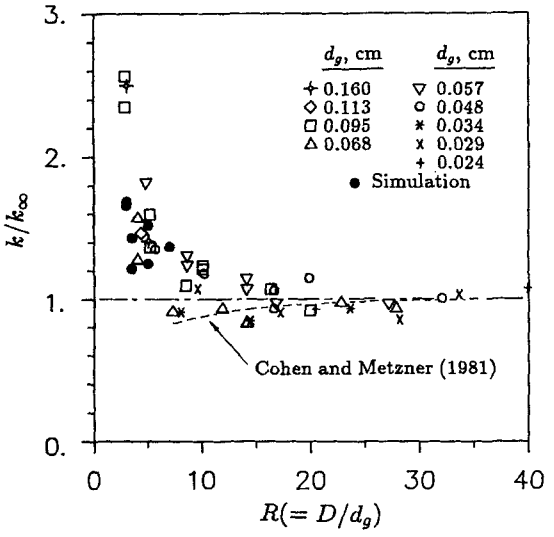

Figure 10. Dependence of permeability on D/d_g.

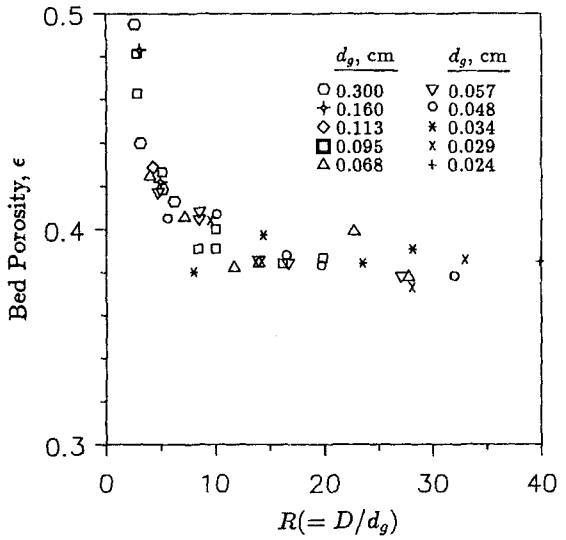

Figure 11. Dependence of bed porosity on D/d_g.

found to decrease with decreasing R if R is larger than around 7 or 8. The broken line in Figure 10 shows the predictions of a parallel capillary tubes model (Cohen and Metzner, 1981), which are supported by experimental data from various sources in the literature. Does it mean that there is a major conflict between this and previous studies? The difference can be reconciled as follows.

As pointed out in connection with Figure 6, the geometrical characteristics of the packed tube suggest that the wall effect has two opposite and competing effects on flow in slim packed beds. The higher porosity in the wall zone can promote fluid flow, but the higher surface area per unit volume can have a retarding effect. As suggested by Nield (1983) and in a discussion between Cohen and Nield (1985), whether k/k_∞ is greater or less than unity depends on which is the dominant factor. For R between about 7 and 30, our data indicate that it indeed can go either way. We found that for a fixed R value, a tube with a lower bed porosity generally resulted in a lower k/k_∞ value. This can be seen in Table 1 for four repeated experiments. This leads us to conclude that the two competing factors are in close contention in this region of R and slight variations in bed porosity can decide which one dominates over the other. And we speculate that the observation of decreasing k/k_∞ with decreasing R is due to packings with more or less the same bed porosity as in the previous studies. We did not make special efforts to pack our tubes. Thus, the data hover around unity until the increase in bed porosity is so large that k/k_∞ shows a definite positive deviation from unity.

The solid circles in Figure 10 are the data from computer sim-

Table 1. Dependence of Apparent Permeability on Bed Porosity

D cm	d_g cm	R	Run 1 ϵ	Run 1 k/k_∞	Run 2 ϵ	Run 2 k/k_∞
0.273	0.095	2.9	0.482	2.56	0.462	2.35
0.491	0.057	8.6	0.410	1.31	0.407	1.24
0.957	0.095	10.1	0.391	1.23	0.387	1.21
0.802	0.034	23.6	0.394	1.01	0.386	0.93

ulation. Four different values of R were used: 3, 3.5, 5, and 7. The square tubes were all 10 particle radii in height. Except for $R = 7$, the other three cases were repeated for tubes 20 particle radii in height. The number of simulation data points is somewhat limited because each realization requires a significant amount of effort. In addition, G in Eq. 23 for the 14 × 14 × 10 sphere pack is a 1,189 × 1,189 matrix and it becomes too large for the computer available to us when R is larger than seven. Nonetheless, it can be seen that the simulation data are in general agreement with the experimental data. It should be mentioned that in calculating the permeability for flow in the four square tubes with Eq. 1, the cross-sectional areas are 28, 41, 92, and 188, respectively, in units of the particle radius squared. In essence, eight units are taken out from each to account for the fact that the space at the four corners does not participate in the flow simulation.

The computer simulation allows us to examine flow through individual channels. Figure 12 shows the distribution of the volumetric flow rate in the circular sinusoidal tubes in the 10 × 10 × 20 tube. The flow rate has been normalized with the mean value, $\langle q_{ct} \rangle$. The ratio of $q_{ct}/\langle q_{ct} \rangle$ can be as high as 17, but in order to show more clearly the majority of the distribution, the plot is truncated at $q_{ct}/\langle q_{ct} \rangle = 10$, and contains 99.2% of the actual data. Figure 13 shows the distribution of the volumetric flow rate in the triangular sinusoidal tubes in the same 10 × 10 × 20 tube. The mean value of $q_{tt}/\langle q_{ct} \rangle$ is 3.14, indicating that the flow rate in a wall channel is higher than that in the interior of the bed.

Finally, two points regarding Figure 10 need to be discussed. We invoked the pseudosteady assumption in Eq. 24. It is therefore useful to examine the Reynolds numbers ($Re = \rho d_g Q/A\mu$) in our experiments. As discussed, each experiment begins with a given hydrostatic head, which decreases as the water levels in the two burettes approach each other. Thus, the Reynolds number is the highest at the beginning of each run and decreases as the flow slows down. Of the different combinations of tubes and particle sizes, large tubes and large spheres would lead to a higher flow rate than small tubes and small spheres. The highest Reynolds number in all the experiments was obtained with the 1.890 cm tube packed with 0.095 cm spheres. The Reynolds number at flow start-up was 1.11 and ended at 0.14. The lowest was obtained with the 0.273 cm tube packed with 0.029 cm spheres. The Reynolds number at flow start-up was 0.054 and ended at 0.032.

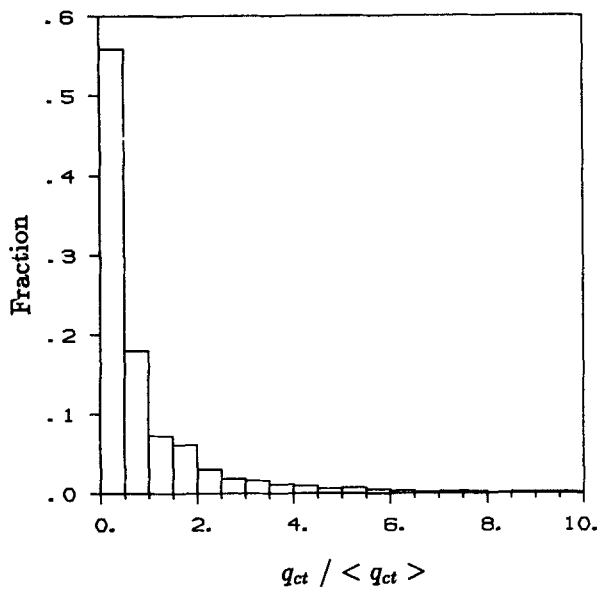

Figure 12. Histogram of volumetric flow rate through a circular sinusoidal tube.

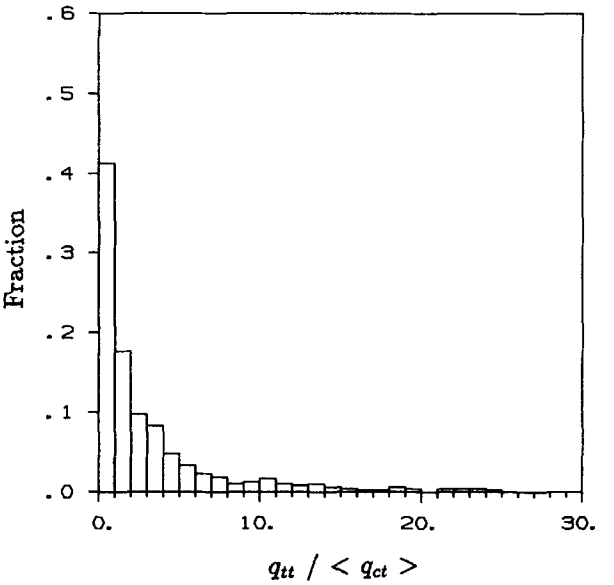

Figure 13. Histogram of volumetric flow through a triangular sinusoidal tube.

Also, our spheres were not exactly of a uniform size. The reported particle size is actually the mean value of the maximum size and minimum size in that lot. A key question is what mean size should be used in Eq. 33 to calculate k/k_∞. The arithmetic mean might not be appropriate for two reasons. First, experience shows that there are more small spheres than large ones in any given lot. Second, the small spheres are expected to have more influence on the overall permeability. For lack of better information, we choose $d_g = (2d_{g,\min} + d_{g,\max})/3)$, for which the k/k_∞ values in Figure 10 would be close to unity for R larger than 25. This of course is in agreement with the well-known experimental observation that for such tubes with sufficiently high R, the wall effect on permeability is minimal.

Conclusions

In modeling flow in porous media, models are needed that account for the interaction between the solid matrix and the fluid phase. For this reason, a large number of porous medium models have appeared in the literature. Some models are highly simplified representations of the actual medium so that rigorous and sophisticated fluid flow analysis can be performed. However, in cases such as flow in a slim tube, we believe that the morphology of the porous structure can have a more significant impact on the permeability. This is why we opted for the computer-generated packed tube. Clearly, the trade-off between a realistic porous medium model and a detailed flow analysis depends on the purpose of the study. For instance, an obvious extension of this work is to study the permeability of shaped particles such as cylindrical extrudates in a slim tube. Little is known about the morphology of this system and porous medium modeling should precede flow analysis.

Notation

A = cross-sectional area
A_v = surface area per unit volume
$ABCEFG$ = points in Figure 3
$b = (r_p - r_c)/(r_p + r_c)$
$b' = (r_{ph} - r_{ch})/(r_{ph} + r_{ch})$
$c = (h_{pw} - h_{cw})/(h_{pw} + h_{cw})$
$c' = (h_{pwh} - h_{cwh})/(h_{pwh} + h_{cwh})$
D = tube diameter or width
d_g = particle diameter
d_w = distance from center of a sphere to a wall
f, g = fraction of l for circular, triangular sinusoidal tubes
G = conductance matrix
g = conductance
h = height of an equilateral triangle
i, j = dummy indices
J = equivalent flow rate vector
k = absolute permeability
k_∞ = permeability of an infinite porous medium
L = packing length
l = half of wavelength of a sinusoidal tube
p = pressure
Q = volumetric flow rate through a porous medium
q = volumetric flow rate through a channel
R = ratio of tube diameter to particle diameter
r = radius
S = length
t = time
t_o = initial time
V = volume
x, y, z = Cartesian coordinates

Greek letters

α = combined resistances
Δh = hydrostatic head
ϵ = porosity
μ = dynamic viscosity
ρ = density

Subscripts

b = burette
c = constriction
ct = circular sinusoidal tube
h = hydraulic
p = pore
sl = solid-fluid
t = tetrahedral unit
tt = triangular sinusoidal tube
w = pentahedral unit

Literature Cited

Beavers, G. S., and D. D. Joseph, "Boundary Conditions at a Naturally Permeable Wall," *J. Fluid Mech.*, **30,** 197 (1967).

Benenati, R. F., and C. B. Brosilow, "Void Fraction Distribution in Beds of Spheres," *AIChE J.*, **8,** 359 (1962).

Bird, R. B., W. E. Stewart, and E. N. Lightfoot, *Transport Phenomena,* Wiley, New York (1960).

Chan, S. K., and K. M. Ng, "Geometrical Characteristics of a Computer-Generated Three-Dimensional Packed Column of Equal and Unequal Sized Spheres, with Special Reference to Wall Effects," *Chem. Eng. Commun.*, **48,** 215 (1986).

———, "Geometrical Characteristics of the Pore Space in a Random Packing of Equal Spheres," *Powder Tech.*, **54,** 147 (1988).

Choudhary, M., J. Szekely, and S. W. Weller, "The Effect of Flow Maldistribution on Conversion in a Catalytic Packed-Bed Reactor," *AIChE J.*, **22,** 1021 (1976).

Cohen, Y., and A. B. Metzner, "Wall Effect in Laminar Flow of Fluids through Packed Beds," *AIChE J.*, **27,** 705 (1981).

Cohen, Y., and D. A. Nield, Discussion of Nield's (1983) paper by Cohen, and Nield's reply, *AIChE J.*, **31,** 525 (1985).

Coulson, J. M., "The Flow of Fluids through Granular Beds: Effect of Particle Shape and Voids in Streamline Flow," *Trans. Inst. Chem. Eng.*, **27,** 237 (1949).

Desoer, C. A., and E. S. Kuh, *Basic Circuit Theory,* McGraw-Hill, New York (1969).

Dixon, A. G., "Thermal Resistance Models of Packed-Bed Effective Heat Transfer Parameters," *AIChE J.*, **31,** 826, (1985).

Dixon, A. G., and D. L. Cresswell, "Theoretical Prediction of Effective Heat Transfer Parameters in Packed Beds," *AIChE J.*, **25,** 663 (1979).

Dixon, A. G., M. A. DiCostanzo, and B. A. Soucy, "Fluid-Phase Radial Transport in Packed Beds of Low Tube-to-Particle Diameter Ratio," *Int. J. Heat Mass Transfer,* **27,** 1701 (1984).

Dullien, F. A. L., "Single-Phase Flow through Porous Media and Pore Structure," *Chem. Eng. J.*, **10,** 1 (1975).

———, *Porous Media—Fluid Transport and Pore Structure,* Academic Press, New York (1979).

Furnas, C. C., "Flow of Gases through Beds of Broken Solids," Bull. U.S. Bur. Mine, No. 307 (1929).

Koplik, J., H. Levine, and A. Lee, "Viscosity Renormalization in the Brinkman Equation," *Phys. Fluid,* **26,** 2864 (1983).

Lahbabi, A., and H. C. Chang, "High Reynolds Number Flow through Cubic Arrays of Spheres. Steady-State Solution and Transition to Turbulence." *Chem. Eng. Sci.*, **40,** 435 (1985).

Larson, R. E., and J. J. L. Higdon, "Microscopic Flow near the Surface of Two-Dimensional Porous Media. 1: Axial Flow," *J. Fluid Mech.*, **166,** 449 (1986).

Lerou, J. J., and G. F. Froment, "Velocity, Temperature and Conversion Profiles in Fixed-Bed Catalytic Reactors," *Chem. Eng. Sci.*, **32,** 853 (1977).

Melanson, M. M., and A. G. Dixon, "Solid Conduction in Low d_t/d_p Beds of Spheres, Pellets, and Rings." *Int J. Heat Mass Transfer,* **28,** 383 (1985).

Mehta, D., and M. C. Hawley, "Wall Effect in Packed Columns," *Ind. Eng. Chem. Process Des. Dev.*, **8,** 280 (1969).

Neale, G. H., and W. K. Nader, "Prediction of Transport Processes within Porous Media: Creeping Flow Relative to a Fixed Swarm of Spherical Particles," *AIChE J.*, **20,** 530 (1974).

Ng, K. M., and A. C. Payatakes, "Critical Evaluation of the Flow Rate-Pressure Drop Relation Assumed in Permeability Models," *AIChE J.*, **31,** 1569 (1985).

Nield, D. A., "Alternative Model for Wall Effect in Laminar Flow of a Fluid through a Packed Column," *AIChE J.*, **29,** 688 (1983).

Payatakes, A. C., and M. A. Neira, "Model of the Constricted Unit Cell Type for Isotropic Granular Media," *AIChE J.*, **23,** 922 (1977).

Payatakes, A. C., C. Tien, and R. M. Turian, "A New Model for Granular Porous Media," *AIChE J.*, **19,** 58 (1973).

Payatakes, A. C., K. M. Ng, and R. W. Flumerfelt, "Oil Ganglion Dynamics During Immiscible Displacement: Model Formulation," *AIChE J.*, **26,** 430 (1980).

Richardson, S., "A Model for the Boundary Condition of a Porous Material. 2," *J. Fluid Mech.*, **49,** 327 (1971).

Rose, H. E., "An Investigation into the Laws of Flow of Fluids through Beds of Granular Materials," *Proc. Inst. Mech. Eng.*, **153,** 141 (1945).

Sheffield, R. E., and A. B. Metzner, "Flow of Nonlinear Fluids through Porous Media," *AIChE J.*, **22,** 736 (1976).

Snyder, L. J., and W. E. Stewart, "Velocity and Pressure Profiles for Newtonian Creeping Flow in Regular Packed Beds of Spheres," *AIChE J.*, **12,** 167 (1966).

Sørensen, J. P., and W. E. Stewart, "Computation of Forced Convection in Slow Flow through Ducts and Packed Beds. II: Velocity Profile in a Simple Cubic Array of Spheres," *Chem. Eng. Sci.*, **29,** 819 (1974).

Taylor, G. I., "A Model for the Boundary Condition of a Porous Material. 1," *J. Fluid Mech.*, **49,** 319 (1971).

van Brakel, J., "Pore Space Models for Transport Phenomena in Porous Media—Review and Evaluation with Special Emphasis on Capillary Liquid Transport," *Powder Tech.*, **11,** 205 (1975).

Vortmeyer, D., and J. Schuster, "Evaluation of Steady Flow Profiles in Rectangular and Circular Packed Beds by a Variational Method," *Chem. Eng. Sci.*, **38,** 1691 (1983).

Wilkinson, D., "Modified Drag Theory of Permeability," *Phys. Fluid,* **28,** 1015 (1985).

Zick, A. A., and G. M. Homsy, "Stokes Flow through Periodic Arrays of Spheres," *J. Fluid Mech.*, **115,** 13 (1982).

Manuscript received June 21, 1988, and revision received Aug. 29, 1988.